Research Article

Novel Fuzzy Neural Nonsingular Terminal Sliding Mode Control of MEMS Gyroscope

Zhe Wang[1] and Juntao Fei [2]

[1]*College of IoT Engineering, Hohai University, Changzhou 213022, China*
[2]*Jiangsu Key Lab of Power Transmission and Distribution Equipment Technology, Changzhou, China*

Correspondence should be addressed to Juntao Fei; jtfei@yahoo.com

This paper attempts to improve the robustness and rapidity of a microgyroscope sensor by presenting a double-loop recurrent fuzzy neural network based on a nonsingular terminal sliding mode controller. Compared with the traditional control method, the proposed strategy can obtain faster dynamic response speed and lower steady-state error with high robustness in the presence of system uncertainties and external disturbances. A nonlinear terminal sliding mode controller is designed to guarantee finite-time high-precision convergence of the sliding surface and meanwhile to eliminate the effect of singularity. Moreover, an exponential approach law is used to accelerate the convergence rate of the system to the sliding surface. For suppressing the chattering, the symbolic function in the ideal sliding mode is replaced by the saturation function. To suppress the effect of model uncertainties and external disturbances, a double-loop recurrent fuzzy neural network is introduced to approximate and compensate system nonlinearities for the gyroscope sensor. At the same time, the double-loop recurrent fuzzy neural network can effectively accelerate the speed of parameter learning by introducing the adaptive mechanism. Simulation results indicate that the control system with the proposed controller is easily implemented, and it has higher tracking precision and considerable robustness to model uncertainties compared with the existing controllers.

1. Introduction

The Micro Electro mechanical system (MEMS) gyroscope is an excellent measuring element for angular velocity sensing in the inertial navigation system due to its outstandingly simple and cheap system integration [1]. For improving the control accuracy of microgyroscope, one has to resolve the cross stiffness and cross damping effects generated by fabrication imperfections to thermal and mechanical noise [2]. In recent years, with the development of intelligent control methods, some advanced control algorithms have been applied to micro-gyroscope control systems. Raman et al. corrected the quadrature error in the digital domain of the gyroscope system with an unconstrained force feedback [3]. Rahmani et al. exploited a sliding PID controller to enhance the robustness of the control system and improve the convergence rate for the reaching stage of the sliding surface

[4]; Fazlyab et al. incorporated an additional interval sliding mode control with parameter estimation to track the resonant frequencies and to eliminate the undesired mechanical couplings [5].

Among the foregoing strategies, the sliding mode control scheme (SMC) has the outstanding properties of fast response, high robustness, and easy implement [6]. Due to these outstanding advantages, sliding mode control suits a wide range of industrial applications, such as spacecraft flights, piezoelectric actuators, autonomous aerial vehicles, and mechatronic motor-table systems. In SMC, the tracking error will converge to zero gradually after the system state trajectory moves to the switching surface [7, 8]. Wang and Yau proposed a nonlinear model of a gyroscope based on the SMC, which can adjust the driving signal of the gyroscope according to the change of its parameters, and ensure that the gyroscope is always in the resonant state [9]. However,

SMC is easily affected by controller chattering caused by structural discontinuity, and a second-order SMC has been proved to eliminate the chattering without reducing the control accuracy in [10]. Subjected to the SMC, time delay compensation has been synthesized into the robust control strategy to provide faster convergence with negligible chattering [11]. Fei and Feng proposed a super-twisting sliding mode control algorithm applied in the gyroscope system, which can weaken the effect of chattering [12]. Although the speed of asymptotic convergence can be controlled by changing the sliding surface parameters, the conventional sliding mode tracking error still has difficulty in arriving to convergence bound in finite time [8]. To solve this problem, Venkataraman and Gulati and Man et al. proposed a terminal sliding mode controller (TSMC) [13, 14]. In the TSMC, the traditional linear sliding mode is replaced by nonlinear sliding mode for accelerating the rate of convergence near the equilibrium point [15]. Applying the advantages of the TSMC in the MEMS gyroscope, Ghanbari and Moghanni-Bavil-Olyaei exhibited faster trajectory tracking speed and estimated the gyroscope parameters with the Kalman filter observer [16]. Adaptive control is synthesized into the double-loop integral terminal sliding mode in [17], which ensured that the position and speed tracking errors of the vehicle could converge to zero in finite time. An adaptive fuzzy-neural fractional-order current controller is introduced in the terminal sliding controller to track ideal current of an active power filter with limited time control performance in [18]. However, because of singularity problem, as the system state happens to be in a specific subspace of the state space, the signal of the terminal sliding mode controller may appear infinite abruptly. Subjected to the TSMC, some scholars designed a nonsingular terminal sliding mode controller (NTSMC). The NTSMC inherits the advantage of finite-time convergence of the TSMC and eliminates the negative exponential term in the control rate, thus avoiding the denominator approaching zero. Ma and Lin verified its engineering applicability in the permanent magnet synchronous motor servo system [19]. Hou et al. applied the NTSMC to the current control system to solve the singularity problem with a fast response [20].

Neural network and fuzzy control are two commonly used methods to solve the control problems in nonlinear systems. RBF neural networks in MEMS systems were used to estimate the unknown upper bound of model uncertainty and external disturbances [21]. Fuzzy control is another control method based on linguistic decision, which shows satisfactory fault tolerance capability and unprecedented parallelism cyclability [22]. Zhu and Fei estimated the upper bound of the error of the disturbance observer with a fuzzy system in a DC-AC inverter [23]. A robust adaptive control strategy using a fuzzy compensator adopted on the MEMS triaxial gyroscope is proposed in [24]. In recent years, some scholars have integrated fuzzy control and neural network control to propose fuzzy neural network (FNN) control for overcoming the nonlinearity and complexity of time-varying systems in practical engineering. Fei and Wang combine FNN control with fractional-order sliding mode control in the current control system for active power filter [25]. Fei

and Liang added fuzzy neural network control to the gyroscope feedback system [26]. Lee and Teng proposed a complex fuzzy neural network structure and expanded the basic ability of the FNN to cope with complicated nonlinear problem [27]. A new output feedback neural structure which has two hidden layers is proposed in [28–30].

In this paper, we proposed a double-loop recurrent fuzzy neural network (DRFNN) of the NTSMC, in which the values of center vector and base width can be stabilized to the optimum value according to the adaptive algorithm designed in the process of parameter learning. At the same time, because the inner and outer signal feedback loop is added, compared with the ordinary FNN, the DRFNN can store more information and has higher accuracy in function approximation. The motivation of this study is to design a high-precision control method for controlling the MEMS gyroscope with fast response speed and high robustness. A NTSMC, which utilizes a nonsingular terminal sliding surface, is developed to accelerate convergence velocity and improve control accuracy. However, despite these advantages, the development of the NTSMC remains hindered by the nonlinear term of the gyroscope sensor. To be insensitive to uncertainties and disturbances, the DRFNN with an adaptive algorithm is synthesized into the NTSMC. The novelties and contributions of the proposed DRFNN of the NTSMC can be addressed in the following aspects:

(1) A NTSMC is established to accelerate the response of the system to converge to the sliding surface; although the system state of the traditional TSMC can converge to origin in finite time, it would cause singular problems in the control process. In this paper, we eliminate the negative exponential term with a nonsingular terminal control rate, thus preventing the singularity fundamentally.

(2) For improving the robustness of the system, the DRFNN is synthesized into the NTSMC to compensate system nonlinearities. The DRFNN has incorporated inner and outer feedback loops to the ordinary FNN structure, which optimizes the network structure and shortens the learning time of parameters so that it can better adapt to the complex nonlinear system model.

This paper is organized as follows. Section 2 describes the dynamics of the MEMS gyroscope, and the mathematical model is also presented here. In Section 3, we adopt the NTSMC into the MEMS gyroscope, where the systematical analysis for the stability and the control performance is carried out, and then the DRFNN scheme with inner and outer feedback loops is formulated in details. Simulation studies are presented in Section 4 to validate the effectiveness by comparing with other existing controllers for the MEMS gyroscope. Section 5 summarizes all the work.

2. Mathematical Model

When the moving point moves relative to a moving reference frame and the moving reference frame rotates at the same time, the point will have Coriolis acceleration. The

working principle of the microgyroscope is to measure the rotation angular velocity of the motion coordinate system relative to the inertial coordinate system indirectly by detecting the vibration caused by the Coriolis acceleration.

Abstract the motion of the particle into two coordinate systems, as shown in Figure 1, where $OX_1Y_1Z_1$ is a moving coordinate system, assuming the direction vector of the coordinate system are i, j, and k, respectively, and $OX_2Y_2Z_2$ is an inertial coordinate system. Suppose the moving coordinate system rotates relative to the inertial coordinate system and the rotational angular velocity is Ω. The distance from the particle m to the origin is denoted as $r(x, y, z)$, which can be regarded as $r = xi + yj + zk$, the relative velocity of the moving coordinate system with respect to the inertial coordinate system is $V_r = i\,dx/dt + j\,dy/dt + k\,dz/dt$, the angle between the velocity V_r and angular velocity Ω is marked as θ, and the Coriolis acceleration caused by the motion of rotation is expressed as $a_k = 2\Omega \times V_r$, whose direction perpendicular to the rotating angular velocity Ω and particle motion direction [31], Figure 2 is a schematic diagram of Coriolis acceleration.

Suppose the mass of the gyroscope is m and the force on the output axis generated by the Coriolis acceleration is denoted as Coriolis inertial force F, the expression is $F = ma_k = 2m\Omega \times v_r$ and its magnitude is proportional to the input angular velocity. Assuming the x-axis direction is the driving mode, y-axis direction is the sensing mode, simplifying the microgyroscope to motion model, as shown in Figure 3, according to the effect of Coriolis acceleration, when the mass m moves harmonically driven by periodic electrostatic force, if the angular velocity input Ω is detected on the z-axis, the mass m will vibrate on the y-axis.

Considering that the presence of angular velocity Ω in the z-axis direction brings about a dynamic coupling between the x-axis and y-axis, we decompose angular velocity into three coordinate axes of x, y, and z, the value of which is Ω_x, Ω_y, and Ω_z, respectively. Referring to [32], there is an ideal assumption that the gyro's rotational velocity Ω_z remains constant over a sufficiently long period and the differential equation of the x-axis and y-axis can be regarded as follows:

$$\begin{cases} m\ddot{x} + d_x\dot{x} + \left[k_x - m\left(\Omega_y^2 + \Omega_z^2\right)\right]x + m\Omega_x\Omega_y y \\ \quad = u_x + 2m\Omega_z\dot{y}, \\ m\ddot{y} + d_y y + \left[k_y - m\left(\Omega_y^2 + \Omega_z^2\right)\right]y + m\Omega_x\Omega_y x \\ \quad = u_y - 2m\Omega_z\dot{x}, \end{cases} \tag{1}$$

where d_x and d_y are the damping coefficients; k_x and k_y are the spring coefficients, respectively; Ω_x, Ω_y, and Ω_z are the angular rate components along each axis of the gyroscope frame; and u_x and u_y are electrostatic forces in x and y directions.

In the actual manufacturing process, the structure of the microgyroscope is not completely symmetric because of fabrication imperfections, so there will be additional dynamic coupling between x-axis and y-axis. In this case, even without angular velocity input, the system will still have output error of angular velocity. Taking the above factors into consideration, (1) can be rewritten as
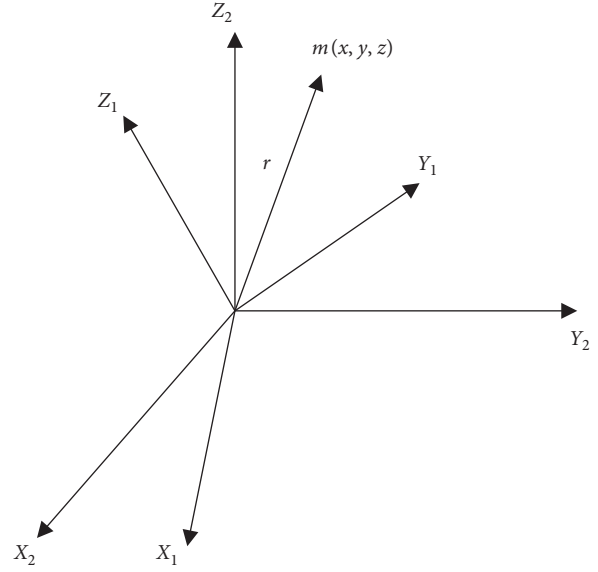

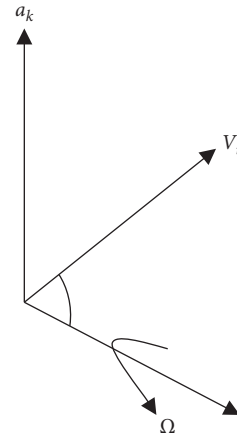FIGURE 1: The coordinate system of the motion of the particle.

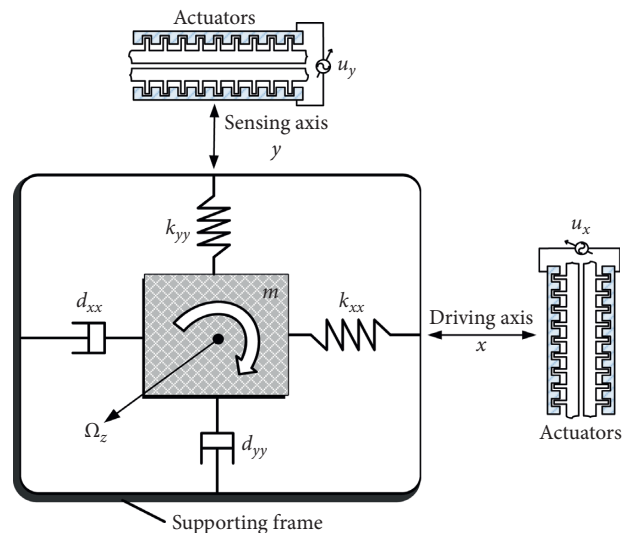FIGURE 2: A schematic diagram of Coriolis acceleration.

FIGURE 3: Simplified motion model of the MEMS gyroscope.

$$\begin{cases} m\ddot{x} + d_{xx}\dot{x} + d_{xy}\dot{y} + k_{xx}x + k_{xy}y = u_x + 2m\Omega_z\dot{y}, \\ m\ddot{y} + d_{xy}\dot{x} + d_{yy}\dot{y} + k_{xy}x + k_{yy}y = u_y - 2m\Omega_z\dot{x}, \end{cases} \quad (2)$$

where k_{xy} and d_{xy} are the coupling spring coefficient and coupling damping coefficient caused by the asymmetries of suspension structure. Although these two parameters are unknown, they do not affect the accuracy of the model because they are too small compared with the proof mass. Meanwhile, Ω_x and Ω_y are also treated as unknown components of spring terms.

Considering that there is a big time-scale difference between the input angular velocity and the self-resonant frequency of the microgyroscope, we deal with the equation in a nondimensionalized way for numerical simulation.

The nondimensionalized model is as follows:

$$\begin{cases} \ddot{x} + d_{xx}\dot{x} + d_{xy}\dot{y} + \omega_x^2 x + \omega_{xy}y = u_x + 2\Omega_z\dot{y}, \\ \ddot{y} + d_{xy}\dot{x} + d_{yy}\dot{y} + \omega_{xy}x + \omega_y^2 y = u_y - 2\Omega_z\dot{x}, \end{cases} \quad (3)$$

where

$$\frac{d_{xy}}{m\omega_0} \longrightarrow d_{xy}, \frac{u_x}{m\omega_0^2 q_0} \longrightarrow u_x, \frac{u_y}{m\omega_0^2 q_0} \longrightarrow u_y,$$

$$\frac{k_{xx}}{m\omega_0^2} \longrightarrow \omega_x^2, \frac{k_{xy}}{m\omega_0^2} \longrightarrow \omega_{xy}, \frac{k_{yy}}{m\omega_0^2} \longrightarrow \omega_y^2, \frac{\Omega_z}{\omega_0} \longrightarrow \Omega_z,$$

$$(4)$$

where m, q_0, and ω_0 are reference mass, reference length, and natural resonance frequency, respectively, and Ω_z is the unknown constant angular velocity.

For the convenience of the expression, we transform the expression equivalently and get the following form:

$$\ddot{q} + D\dot{q} + Kq = u - 2\Omega\dot{q} + d(t), \quad (5)$$

where

$$q = \begin{bmatrix} x \\ y \end{bmatrix}, D = \begin{bmatrix} d_{xx} & d_{xy} \\ d_{xy} & d_{yy} \end{bmatrix}, K = \begin{bmatrix} \omega_x^2 & \omega_{xy} \\ \omega_{xy} & \omega_y^2 \end{bmatrix}, u = \begin{bmatrix} u_x \\ u_y \end{bmatrix},$$

$$\Omega = \begin{bmatrix} 0 & -\Omega_z \\ \Omega_z & 0 \end{bmatrix},$$

$$(6)$$

where D, K, and Ω are unknown parameters that changes over time, $d(t)$ is the external disturbance, and it is bounded by a positive constant L as $|d(t)| \le L$.

3. Nonsingular Terminal Sliding Mode Control

For the microgyroscope system, how to maintain the stability of the driving shaft excitation signal is the key to ensure the accuracy of measurement [33]. In order to generate a constant excitation condition, we assume that the microgyroscope follows an ideal oscillator $q_m(t)$ as the reference signal. In this paper, we design a double-loop recurrent fuzzy neural network (DRFNN) of nonsingular terminal sliding mode control (NTSMC) to make the trajectory of the real gyroscopes $q(t)$ follow that of the reference signal $q_m(t)$; meanwhile, we also

use the DRFNN to estimate the unknown lumped uncertainties for compensating system nonlinearities. The sliding surface of the nonsingular terminal is denoted as follows:

$$s = e + \frac{1}{\beta}\dot{e}^{p/q}, \quad (7)$$

where $s = \begin{bmatrix} s_1 & s_2 \end{bmatrix}$, $e = q_m - q = \begin{bmatrix} q_{m1} - q_1 & q_{m2} - q_2 \end{bmatrix}$ stands for tracking error, $\beta = \begin{bmatrix} \beta_1 & \beta_2 \end{bmatrix}$ is a sliding surface constant, and p and q are both positive odd and they satisfy $1 < p/q < 2$.

Taking the derivative of the sliding surface function yields

$$\dot{s} = \dot{e} + \frac{1}{\beta}\frac{p}{q}\dot{e}^{(p/q)-1}(\ddot{q}_m - \ddot{q}). \quad (8)$$

From (5), we can get that

$$\ddot{q} = f(q,t) + u + d(t), \quad (9)$$

where $f = \begin{bmatrix} f_1 & f_2 \end{bmatrix}^T = -(D\dot{q} + 2\Omega\dot{q} + K_b q)$, which represents the matched lumped uncertainty, and $u = \begin{bmatrix} u_1 & u_2 \end{bmatrix}$ is controllable electrostatic force.

Assuming that the lumped uncertainty $f(q,t)$ is bounded, taking equation (9) into (8), we obtain

$$\dot{s} = \dot{e} + \frac{1}{\beta}\frac{p}{q}\dot{e}^{(p/q)-1}(\ddot{q}_m - f(q,t) - u - d(t)). \quad (10)$$

In order to get $\dot{s} = 0$ and speed up the convergence of the system state to the sliding surface, the exponential control rate is synthesized into the controller. The controller is designed as follows:

$$u = \ddot{q}_m - f(q,t) + \beta\frac{q}{p}\dot{e}^{2-(p/q)} + (L+\eta)\text{sgn}(s) + \eta's, \quad (11)$$

where η and η' are constant matrix in exponential reaching rates.

Substituting control rate (11) into equation (10), we can obtain

$$\dot{s} = \frac{1}{\beta}\frac{p}{q}\dot{e}^{(p/q)-1}(-(L+\eta)\text{sgn}(s) - d(t) - \eta's). \quad (12)$$

For proving the stability of the sliding mode control system, a Lyapunov function is selected as follows:

$$V_1 = \frac{1}{2}s^2. \quad (13)$$

Taking the derivative of V_1 with respective to time, we obtain

$$\dot{V}_1 = s\dot{s} = -\frac{1}{\beta}\frac{p}{q}\dot{e}^{(p/q)-1}[(L+\eta)\text{sgn}(s) + d(t) + \eta's]s$$

$$\le -\frac{1}{\beta}\frac{p}{q}\dot{e}^{(p/q)-1}[(\eta + L - d(t))|s| + \eta's^2]$$

$$\le -\frac{1}{\beta}\frac{p}{q}\dot{e}^{(p/q)-1}(\eta|s| + \eta's^2) = -\frac{1}{\beta}\frac{p}{q}\dot{e}^{(p/q)-1}|s|(\eta + \eta'|s|).$$

$$(14)$$

Since $\eta > 0$, $\eta' > 0$, and p and q are both odd, we get that $\dot{e}^{(p/q)-1} > 0$, so it can be concluded that $\dot{V}_1 \le 0$. According to

the Lyapunov stability criterion, the nonsingular terminal sliding mode $s = 0$ can be reached in finite time, despite of the uncertainty $d(t)$.

Assuming the following boundedness,

$$\frac{1}{\beta} \frac{p}{q} \dot{e}^{(p/q)-1} \left(\eta + \eta' |s| \right) > \varepsilon, \tag{15}$$

where $\varepsilon > 0$, so it can be concluded that

$$\dot{V}_1 \leq -\varepsilon |s| = -\varepsilon \sqrt{V_1}. \tag{16}$$

(16) can be rewritten as

$$\frac{dV_1}{\sqrt{V_1}} \leq -\sqrt{2} \varepsilon \, dt. \tag{17}$$

Denoting the t_r as the total time from the initial state to $s(t) = 0$, taking the integral of (17) with respect to time, we obtain

$$\int_{V_1(0)}^{V_1(t_r)} \frac{dV_1}{\sqrt{V_1}} \leq -\sqrt{2} \int_0^{t_r} \varepsilon \, dt. \tag{18}$$

We can deduce the t_r as

$$t_r \leq \frac{\sqrt{2 \left(V_1(0) - V_1(t_r) \right)}}{\varepsilon}. \tag{19}$$

Now we prove that $s = 0$ will be reached from any initial state $\dot{e}(0)$ in finite time.

When the system state reaches the sliding mode surface, according to $s = e + (1/\beta)\dot{e}^{p/q} = 0$, the tracking error will converge to zero in t_c time. t_c can be calculated as $t_c = p/(p-q)\beta e_{(t_r)}^{1-(q/p)}$. So, the system state can reach the sliding mode surface from any initial state and converge to the equilibrium point in a finite period of time.

4. Double-Loop Recurrent Fuzzy Neural Network of Nonsingular Terminal Sliding Mode Control

Because D, K, and Ω in (5) change with time and they cannot be accurately obtained, it is difficult to obtain the uncertainties $f(q, t)$ in the gyroscope system, so the application of controller (11) in engineering is not practicable. Considering that the neural network can compensate for nonlinear terms, the double-loop recurrent fuzzy neural network (DRFNN) can be used to compensate unknown model uncertainties.

Since the conventional neural network with fixed base width and center vector lacks adaptive adjustment mechanism in the face of different input signals, for adapting to the complex nonlinear system model of the microgyroscope, a double-loop recurrent fuzzy neural network (DRFNN), as shown in Figure 4, is proposed in this paper, which is a three-layer fuzzy neural network embedded with double closed-loop dynamic feedback connection. The first layer is the input layer, which is composed of the signal receiving nodes. It adds the outer feedback loop to the basis of the traditional fuzzy neural network structure, so the nodes in the input layer can receive the output signals fed back by the signals

from the output layer. The second layer is the membership layer. The nodes in this layer are responsible for the calculation of the membership function. At the same time, the signals of the previous step will be fed back to the nodes in this layer through the inner feedback network. The third layer is the output layer, which completes the calculation of the signals transmitted by the fuzzy layer. The output signals are transmitted back to the nodes of the input layer through the outer feedback loop.

Next, specific functions of the input layer, membership layer, and output layer are introduced as follows.

4.1. First Layer: Input Layer. The input layer of the DRFNN realizes the transmission of the input signal $X = \begin{bmatrix} x_1 & x_2 & \cdots & x_m \end{bmatrix}^T$ and receives the output signal exY of the previous step back through the outer closed loop. The output layer is associated with the input layer by the outer gain W_{rom}. Supposing the output signal of the input layer is $\theta = \begin{bmatrix} \theta_1 & \theta_2 & \cdots & \theta_m \end{bmatrix}^T$, where m is the total number of the linguistic variables:

$$\theta_m = x_m W_{\mathrm{rom}} exY. \tag{20}$$

4.2. The Second Layer: Membership Layer. The Gaussian basis function is presented as the membership function, and the nodes of the membership layer complete the calculation of the Gaussian function. In this layer, the inner closed loop structure is added on the basis of the traditional FNN membership layer structure. The nodes of this layer will feed back the results of the previous Gaussian function calculation to the input layer and calculate the Gaussian basis function together with the nodes of input. Supposing the output of this layer is μ_i, which can be regarded as follows:

$$\mu_i = \exp \left[-\frac{\left\| \theta \cdot r_i \cdot ex\mu_i - c_i \right\|^2}{b_i^2} \right], \tag{21}$$

where r_i is the feedback gain of the inner layer, c_i is the center vector, and b_i is the basis width.

4.3. The Third Layer: Output Layer. The output layer node and each node in the membership layer are associated by weight $W = \begin{bmatrix} W_1 & W_2 & \cdots & W_k \end{bmatrix}$. The signal nodes of the output layer are labeled as Y, which represent the summation of all input signals:

$$Y = \sum_{k=1}^n W_k h_k = W_1 h_1 + W_2 h_2 + \cdots + W_n h_n. \tag{22}$$

Meanwhile, the output layer node feed back to the input layer nodes through the outer closed loop, and the feedback signal is denoted as exY.

Figure 5 shows the block diagram of the DRFNN of NTSMC based on the microgyroscope, where the DRFNN is used to predict and compensate the nonlinear terms of the system.
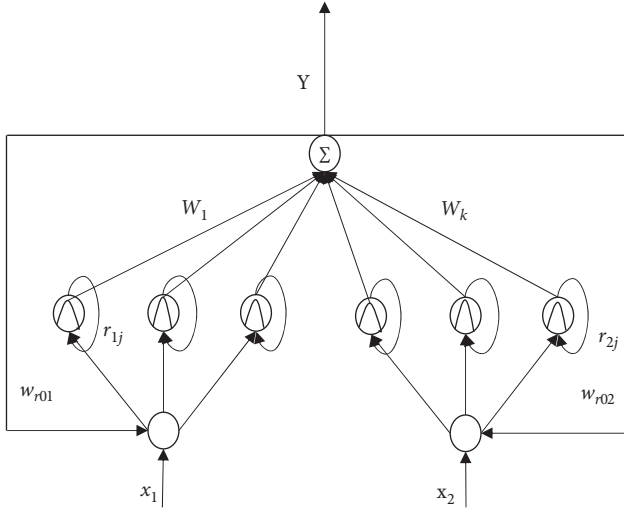
Suppose the output of the DRFNN can be parameterized as

FIGURE 4: The mode of the DRFNN.

$$\widehat{\Gamma}(q) = \widehat{W}^T \widehat{l}, \qquad (23)$$

where $\widehat{W}$ represents the estimated value of weighting matrix of the DRFNN and $\widehat{l}$ is the estimated output vector of the membership layer, which can be regarded as

$$\widehat{l} = \widehat{l}\left(q, \widehat{c}, \widehat{b}, \widehat{r}, \widehat{W}_{ro}\right). \qquad (24)$$

In (24), we assumed all DRFNN centers, widths, and inner and outer gain can be estimated adequately.

According to Taylor's formula, the $\widetilde{l}$ can be calculated as follows:

$$\widetilde{l} = \frac{\partial l}{\partial c}\bigg|_{c=\widehat{c}} (c^* - \widehat{c}) + \frac{\partial l}{\partial b}\bigg|_{b=\widehat{b}} \left(b^* - \widehat{b}\right) + \frac{\partial l}{\partial r}\bigg|_{r=\widehat{r}}$$

$$\cdot (r^* - \widehat{r}) + \frac{\partial l}{\partial W_{ro}}\bigg|_{W_{ro}=\widehat{W}_{ro}} \left(W_{ro}^* - \widehat{W}_{ro}\right) + O_h \qquad (25)$$

$$= l_c \cdot \widetilde{c} + l_b \cdot \widetilde{b} + l_r \cdot \widetilde{r} + l_{W_{ro}} \cdot \widetilde{W}_{ro} + O_h,$$

where O_h is the higher order term, $l_c = [\partial l_1/\partial c \ \ \partial l_2 /\partial c ... \partial l_k/\partial c]^T|_{c=\widehat{c}}$

$$l_b = \left[\frac{\partial l_1}{\partial c} \ \ \frac{\partial l_2}{\partial c} \ \ ... \ \ \frac{\partial l_k}{\partial c} \right]^T \bigg|_{b=\widehat{b}},$$

$$l_r = \left[\frac{\partial l_1}{\partial r} \ \ \frac{\partial l_2}{\partial r} \ \ ... \ \ \frac{\partial l_k}{\partial r} \right]^T \bigg|_{r=\widehat{r}}, \qquad (26)$$

$$l_{W_{ro}} = \left[\frac{\partial l_1}{\partial W_{ro}} \ \ \frac{\partial l_2}{\partial W_{ro}} \ \ ... \ \ \frac{\partial l_k}{\partial W_{ro}} \right]^T \bigg|_{W_{ro}=\widehat{W}_{ro}}.$$

We make the following assumption prior further discussion.

Assumption 1. The uncertainties of the system $f(q)$ can be described by the optimal weight W^*, the optimal center vector c^*, the optimal widths b^*, the optimal inner feedback gain r^*, and the optimal outer feedback gain W_{ro}^* as follows:

$$\Gamma(q) = W^{*T} l^* + \varepsilon, \qquad (27)$$

where $l^* = l^*(x, c^*, b^*, r^*, W_{ro}^*)$ and $\varepsilon > 0$ is the mapping error, which is assumed to be bounded.

Based on assumption 1, the deviation between the uncertainty $\Gamma(q)$ and the estimated value $\widehat{\Gamma}(q)$ can be regarded as

$$\begin{aligned} \Gamma(q) - \widehat{\Gamma}(q) &= W^{*T} l^* - \widehat{W}^T \widehat{l} + \varepsilon \\ &= W^{*T} (\widehat{l} + \widetilde{l}) - \widehat{W}^T \widehat{l} + \varepsilon \\ &= W^{*T} \widehat{l} + W^{*T} \widetilde{l} - \widehat{W}^T \widehat{l} + \varepsilon \\ &= \widetilde{W}^T \widehat{l} + \widehat{W}^T \widetilde{l} + \widetilde{W}^T \widetilde{l} + \varepsilon \\ &= \widetilde{W}^T \widehat{l} + \widehat{W}^T \widetilde{l} + \varepsilon_0, \end{aligned} \qquad (28)$$

where $\widetilde{w} = w^* - \widehat{w}$ is the weighting matrix error between the optimal value and the current estimated value.

Suppose ε_0 is the approximate error, regarded as $\varepsilon_0 = \widetilde{W}^T \widetilde{l} + \varepsilon$.

Replacing $f(x)$ in (11) by $\widehat{\Gamma}(x)$, we can get a new control law as follows:

$$U = \ddot{q}_m - \widehat{\Gamma}(q) + \beta \frac{q}{p} \dot{e}^{2-(p/q)} + (L + \eta)\text{sgn}(s) + \eta' s. \qquad (29)$$

Theorem 1. *If the modified control law (29), with the nonsingular terminal sliding surface (7) and the adaptive law of the DRFNN designed as (30)–(34), is applied to the gyroscope system defined by (5), then the system's tracking error can converge to origin in a finite time, and the unknown system uncertainties can be estimated online by the DRFNN with high robustness:*

$$\dot{\widehat{W}} = \eta_1 \frac{1}{\beta} \frac{p}{q} \dot{e}^{(p/q)-1} s\widehat{l}, \qquad (30)$$

$$\dot{\widehat{c}}^T = \eta_2 \frac{1}{\beta} \frac{p}{q} \dot{e}^{(p/q)-1} s\widehat{W}^T l_c, \qquad (31)$$

$$\dot{\widehat{b}}^T = \eta_3 \frac{1}{\beta} \frac{p}{q} \dot{e}^{(p/q)-1} s\widehat{W}^T l_b, \qquad (32)$$

$$\dot{\widehat{r}}^T = \eta_4 \frac{1}{\beta} \frac{p}{q} \dot{e}^{(p/q)-1} s\widehat{W}^T l_r, \qquad (33)$$

$$\dot{\widehat{W}}_{ro}^T = \eta_5 \frac{1}{\beta} \frac{p}{q} \dot{e}^{(p/q)-1} s\widehat{W}^T l_{W_{ro}}, \qquad (34)$$

where $\eta_1, \eta_2, \eta_3, \eta_4,$ and η_5 are all positive gains.

Proof. Select the second Lyapunov function as

$$\begin{aligned} V_2 = \frac{1}{2}S^2 &+ \frac{1}{2\eta_1} tr\left(\widetilde{W}^T \widetilde{W}\right) + \frac{1}{2\eta_2} tr\left(\widetilde{c}^T \widetilde{c}\right) + \frac{1}{2\eta_3} tr\left(\widetilde{b}^T \widetilde{b}\right) \\ &+ \frac{1}{2\eta_4} tr\left(\widetilde{r}^T \widetilde{r}\right) + \frac{1}{2\eta_5} tr\left(\widetilde{W}_{ro}^T \widetilde{W}_{ro}\right), \end{aligned}$$
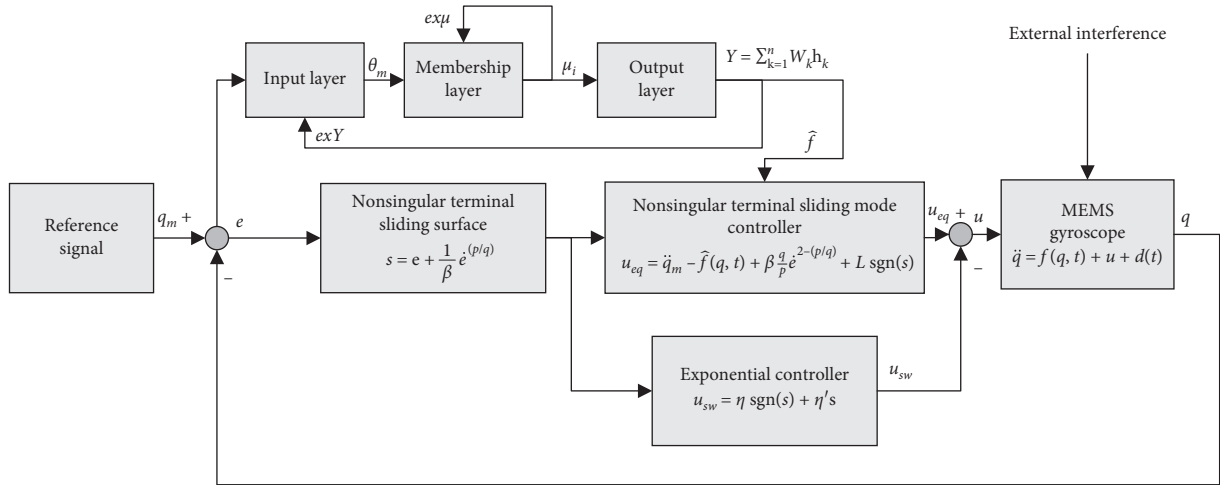
$$(35)$$

where $tr(\cdot)$ denotes the matrix trace operator.

Figure 5: The block diagram of the DRFNN of NTSMC based on the MEMS gyroscope system.

Denoting

$$\frac{1}{2\eta_1}tr\left(\widetilde{W}^T\widetilde{W}\right) + \frac{1}{2\eta_2}tr\left(\widetilde{c}^T\widetilde{c}\right) + \frac{1}{2\eta_3}tr\left(\widetilde{b}^T\widetilde{b}\right) + \frac{1}{2\eta_4}tr\left(\widetilde{r}^T\widetilde{r}\right)$$

$$+ \frac{1}{2\eta_5}tr\left(\widetilde{W}_{ro}^T\widetilde{W}_{ro}\right) = M.$$

(36)

Take the time derivative of V_2 and substitute control law (29) into (35):

$$\dot{V}_2 = S\dot{S} + \dot{M}$$

$$= \frac{1}{\beta}\frac{p}{q}\dot{e}^{(p/q)-1}s\left[\widehat{\Gamma}(x) - \Gamma(x) - d(t)\right.$$

$$\left. - (L + \eta)sgn(s) - \eta's\right] + \dot{M}.$$

(37)

Substitute equation (28) into equation (37) to obtain

$$\dot{V}_2 = \frac{1}{\beta}\frac{p}{q}\dot{e}^{(p/q)-1}s\left[-\left(\widetilde{W}^T\widehat{l} + \widehat{W}^T\widetilde{l} + \varepsilon_0\right) - d(t)\right.$$

$$\left. - (L + \eta)sgn(s) - \eta's\right] + \dot{M}.$$

(38)

Substituting Taylor's expansion of $\widehat{l}$ into the above equation, we get that

$$\dot{V}_2 = -\frac{1}{\beta}\frac{p}{q}\dot{e}^{(p/q)-1}s\widetilde{W}^T\widehat{l} - \frac{1}{\beta}\frac{p}{q}\dot{e}^{(p/q)-1}s\widehat{W}^T\left(l_c\widetilde{c} + l_b\cdot\widetilde{b} + l_r\widetilde{r}\right.$$

$$\left. + l_{W_{ro}}\cdot\widetilde{W}_{ro} + O_h\right) - \frac{1}{\beta}\frac{p}{q}\dot{e}^{(p/q)-1}s\left[\varepsilon_0 + d(t)\right.$$

$$\left. + (L + \eta)sgn(s) + \eta's\right] + \frac{1}{\eta_1}tr\left(\widetilde{W}^T\dot{\widetilde{W}}\right) + \frac{1}{\eta_2}tr\left(\dot{\widetilde{c}}^T\widetilde{c}\right)$$

$$+ \frac{1}{\eta_3}tr\left(\dot{\widetilde{b}}^T\widetilde{b}\right) + \frac{1}{\eta_4}tr\left(\dot{\widetilde{r}}^T\widetilde{r}\right) + \frac{1}{\eta_5}tr\left(\dot{\widetilde{W}}_{ro}^T\widetilde{W}_{ro}\right).$$

(39)

Substituting adaptation laws (30)–(34) into (39), we can obtain

$$-\frac{1}{\beta}\frac{p}{q}\dot{e}^{(p/q)-1}s\widetilde{W}^T\widehat{l} + \frac{1}{\eta_1}tr\left(\widetilde{W}^T\dot{\widetilde{W}}\right) = 0,$$

$$-\frac{1}{\beta}\frac{p}{q}\dot{e}^{(p/q)-1}s\widehat{W}^Tl_c\widetilde{c} + \frac{1}{\eta_2}tr\left(\dot{\widetilde{c}}^T\widetilde{c}\right) = 0,$$

$$-\frac{1}{\beta}\frac{p}{q}\dot{e}^{(p/q)-1}s\widehat{W}^Tl_b\widetilde{b} + \frac{1}{\eta_3}tr\left(\dot{\widetilde{b}}^T\widetilde{b}\right) = 0, \quad (40)$$

$$-\frac{1}{\beta}\frac{p}{q}\dot{e}^{(p/q)-1}s\widehat{W}^Tl_r\widetilde{r} + \frac{1}{\eta_4}tr\left(\dot{\widetilde{r}}^T\widetilde{r}\right) = 0,$$

$$-\frac{1}{\beta}\frac{p}{q}\dot{e}^{(p/q)-1}s\widehat{W}^Tl_{W_{ro}}\widetilde{W}_{ro} + \frac{1}{\eta_5}tr\left(\dot{\widetilde{W}}_{ro}^T\widetilde{W}_{ro}\right) = 0.$$

Then, the $\dot{V}_2$ can be written as follows:

$$\dot{V}_2 = -\frac{1}{\beta}\frac{p}{q}\dot{e}^{(p/q)-1}s\left[\varepsilon_0 + O_{h0} + d(t) + (L + \eta)sgn(s) + \eta's\right]$$

$$= -\frac{1}{\beta}\frac{p}{q}\dot{e}^{(p/q)-1}s\left(\varepsilon_0 + O_{h0} + \eta's\right) - \frac{1}{\beta}\frac{p}{q}\dot{e}^{(p/q)-1}\eta|s|$$

$$- \frac{1}{\beta}\frac{p}{q}\dot{e}^{(p/q)-1}\left(L|s| + d(t)s\right)$$

$$\leq -\frac{1}{\beta}\frac{p}{q}\dot{e}^{(p/q)-1}s\left(\varepsilon_0 + O_{h0} + \eta's\right) - \frac{1}{\beta}\frac{p}{q}\dot{e}^{(p/q)-1}\eta|s|$$

$$\leq -\frac{1}{\beta}\frac{p}{q}\dot{e}^{(p/q)-1}\left[|s|\left(\eta - \left(\varepsilon_0 + O_{h0}\right)\right) + \eta's^2\right].$$

(41)

Then, two different cases will be discussed as follows:

(1) When $s > 0$, we can get $\dot{V}_2$ as

$$\dot{V}_2 = -\frac{1}{\beta}\frac{p}{q}\dot{e}^{(p/q)-1}|s|\left[(\varepsilon_0 + O_{h0} + \eta) + (L + d(t)) + \eta'|s|\right].$$

(42)

Since the external disturbance $d(t)$ is bounded by $|d(t)| \leq L$, whether $d(t)$ is positive or negative, we can always obtain $L + d(t)$ is a positive scalar. Besides, η' is also a positive constant we set up in advance, under the assumption p and q are both positive vector matrix, it further induces that $\dot{e}^{(p/q)-1} > 0$ and η is bounded in $\eta \geq \varepsilon_E + O_E$, where ε_E and O_E denote maximum eigenvalues of ε_0 and O_{h0}, respectively, and then we can get that $\dot{V}_2 \leq 0$.

(2) When $s < 0$, it satisfies $s = -|s|$, and the $\dot{V}_2$ can be written as

$$\dot{V}_2 = -\frac{1}{\beta}\frac{p}{q}\dot{e}^{(p/q)-1}|s|(\eta - \varepsilon_0 - O_{h0}) - \frac{1}{\beta}\eta'\frac{p}{q}\dot{e}^{(p/q)-1}s^2$$

$$- \frac{1}{\beta}\frac{p}{q}\dot{e}^{(p/q)-1}|s|(L - d(t)).$$

(43)

Similar to case 1, L is the bound of the external disturbance, so it satisfies $L - d(t) > 0$, under the assumption p and q are both positive vector matrix, and $\dot{e}^{(p/q)-1} > 0$ can be guaranteed; so as long as η is bounded in $\eta \geq \varepsilon_E + O_E$, it can also be deduced that $\dot{V}_2 \leq 0$.

$\dot{V}_2$ is negative semidefinite. We can obtain that the trajectory reaches the sliding surface in finite time and remains on the sliding surface. At the same time, it ensures that the V_2, s and the adaptive variables c, b, r, W_{ro}, and W are all bounded. Define the function $\Lambda(t) \equiv (1/\beta)(p/q)\dot{e}^{(p/q)-1}[|s|(\eta - (\varepsilon_0 + O_{h0})) + \eta' s^2] = -\dot{V}_2(t)$.

Then, the integral of $\Lambda(t)$ with respect to time can be expressed as

$$\int_0^t \Lambda(\tau)\mathrm{d}\tau \leq V_2(0) - V_2(t).$$

(44)

As $V_2(0)$ is bounded, we can deduce that

$$\lim_{t \longrightarrow \infty} \int_0^t \Lambda(\tau)\mathrm{d}(\tau) < \infty.$$

(45)

Additionally, $\dot{\Lambda}(t)$ is bounded and it can be obtained from Barbalat's Lemma that $\lim_{t \longrightarrow \infty} \Lambda(t) = 0$. It implies that the nonsingular terminal sliding surface converges to zero as $t \longrightarrow \infty$. Besides, the tracking error also converges to zero as $t \longrightarrow \infty$. In this aspect, the DRFNN of the NTSMC system ensures the asymptotical stability of the gyroscope system. $\square$

5. Simulation Analysis

In order to evaluate the effectiveness of the control strategy designed in this paper, we adopt the following microgyroscope parameters:

$$m = 1.8 \times 10^{-7}\,\mathrm{kg},$$
$$d_{xx} = 1.8 \times 10^{-6}\,\mathrm{Ns/m},$$
$$d_{yy} = 1.8 \times 10^{-6}\,\mathrm{Ns/m},$$
$$d_{xy} = 3.6 \times 10^{-7}\,\mathrm{Ns/m},$$
$$k_{xx} = 63.955\,\mathrm{N/m},$$
$$k_{yy} = 95.92\,\mathrm{N/m},$$
$$k_{xy} = 12.779\,\mathrm{N/m}.$$

(46)

Since the vibration magnitude of the x-axis and y-axis are all submicron, we choose $1\,\mu$m as the reference length q_0. Considering that the natural frequency range commonly used in the microgyroscope is all in KHz, ω_0 is determined as 1 KHz. Assuming the magnitude of unknown angular velocity is $\Omega_z = 100$ rad/s. After equivalent transformation as described in Section 2, nondimensional model parameters of the gyroscope are listed as follows:

$$\omega_x^2 = 355.3,$$
$$\omega_y^2 = 532.9,$$
$$\omega_{xy} = 70.99,$$
$$d_{xx} = 0.01,$$
$$d_{yy} = 0.01,$$
$$d_{xy} = 0.002,$$
$$\Omega_z = 0.1.$$

(47)

In the simulation model, the expected motion trajectories of the two axes are selected as $x_m = \sin(4.17t)$ and $y_m = 1.2\sin(5.11t)$. The initial states of the controlled object are presented as $[0\ 0\ 0\ 0]$. The disturbance $d(t) = [0.5\mathrm{rand}n(1,1); 0.5\mathrm{rand}n(1,1)]$ is white noise signal based on standard normal distribution. In the simulation, the sliding surface constant parameters of the nonsingular terminal surface are selected as $p = 9$, $q = 7$, and $\beta = 0.5$.

In (23), the center vector, basis width, inner layer gain, outer layer gain, and weight of the DRFNN are five fully adjustable parameters. Their initial values are chosen as $c = [-0.01\ -0.005\ 0\ 0.005\ 0.01]$, $b = [1\ 1\ 1\ 1\ 1]$, $r = [-0.2\ 0.05\ 0\ -0.05\ 0.3]$, $W_{r0} = 10$, and $W = [-0.2\ 0.05\ 0 - 0.05 - 0.3]$, and their values can be stabilized to appropriate values according to adaptive laws (30)–(34). In (29), to emphasize the fast response, the sum of the limit of disturbance L and the approach gain η is taken as $\eta'' = 10$; in addition, another approach gain η' is taken as. $\eta' = 10$.

In order to reduce the chattering, we replace the symbolic function $\mathrm{sign}(s)$ in the ideal sliding mode with the saturation function $\mathrm{sat}(s)$, and its expression is
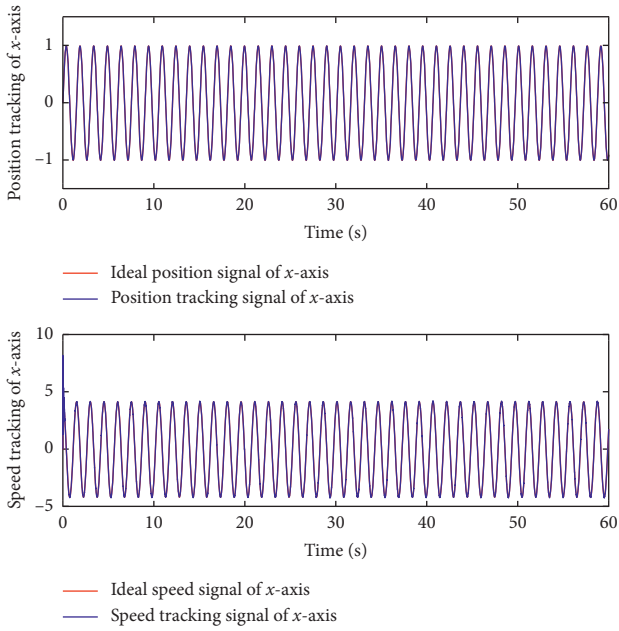
FIGURE 6: Position tracking trajectory and speed tracking trajectory in x-axis.
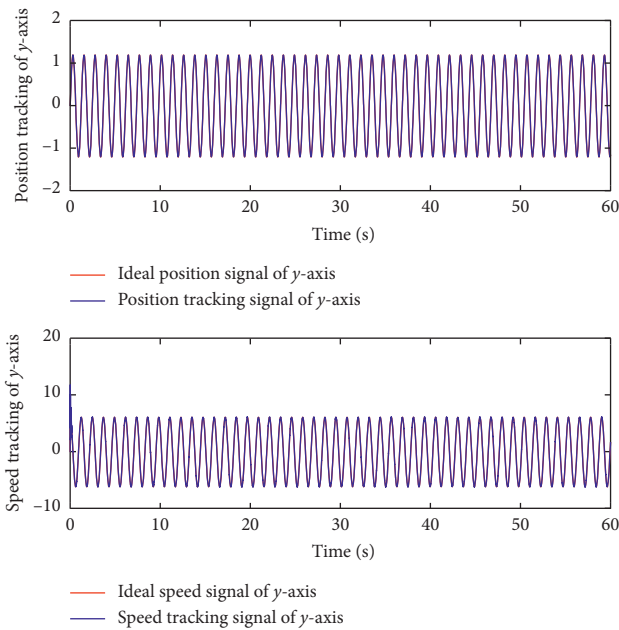

FIGURE 7: Position tracking trajectory and speed tracking trajectory in y-axis.

$$\text{sat}(s) = \begin{cases} 1, & s > \delta, \\ ks, & |s| \le \delta, \\ -1, & s < -\delta, \end{cases} \tag{48}$$

where $k = 1/\delta$ and δ is the boundary layer, and it satisfies $\delta = 0.05$.

The simulation time was set as 60 s, the tracking trajectory and tracking error trajectory of the reference signal are shown in Figures 6–9.
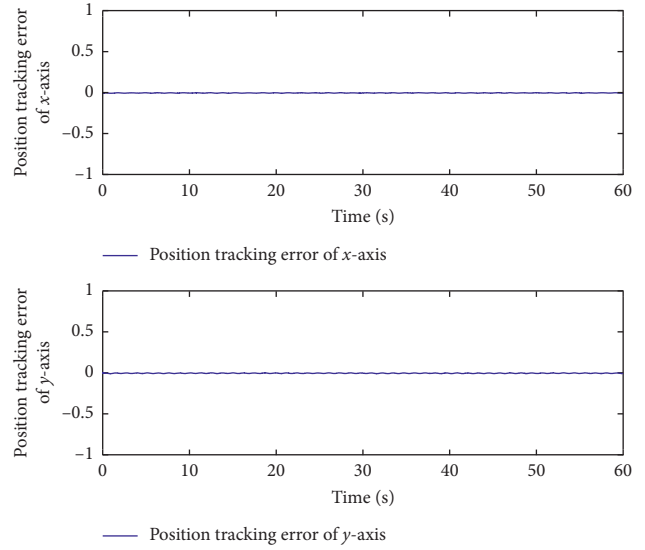
FIGURE 8: Position tracking error.
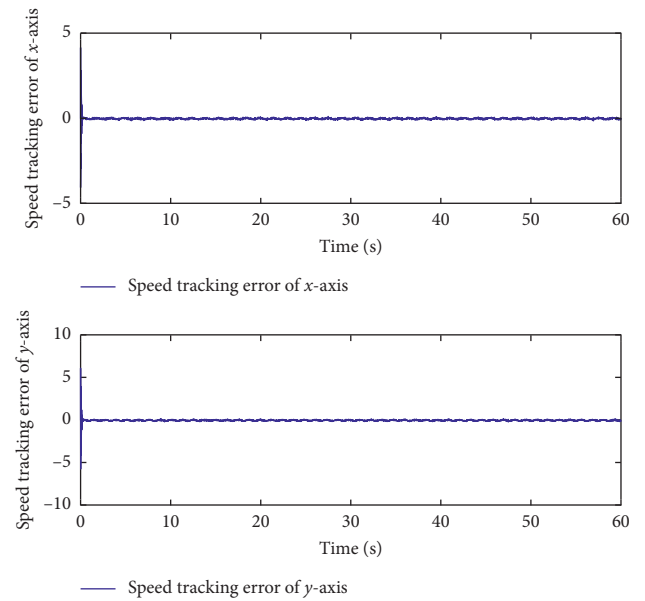
FIGURE 9: Velocity tracking error.

It can be seen from Figures 6–9 that the output of x and y axes can quickly track the input signal in a limited time and the steady-state deviation can be controlled in a very small range.

In order to clearly show the advantages of the DRFNN of NTSMC proposed in this paper, we also investigated the control performance of the FNN of SMC in the simulation for comparison. We use the conventional sliding surface identified as $s = \dot{e} + ke$, where $k = 5$. For ensuring the convergence to the sliding surface, the approach control rate is selected as $u_{sw} = \eta\text{sgn}(s)$, where $\eta = 10$. Meanwhile, the Gaussian basis function is selected as membership function of the FNN as $\mu(x_i) = \exp[-(x_i - c_i)^2/2b^2]$.

The enlarged and comparison figure of the position tracking error is shown in Figure 10, proving the trajectory
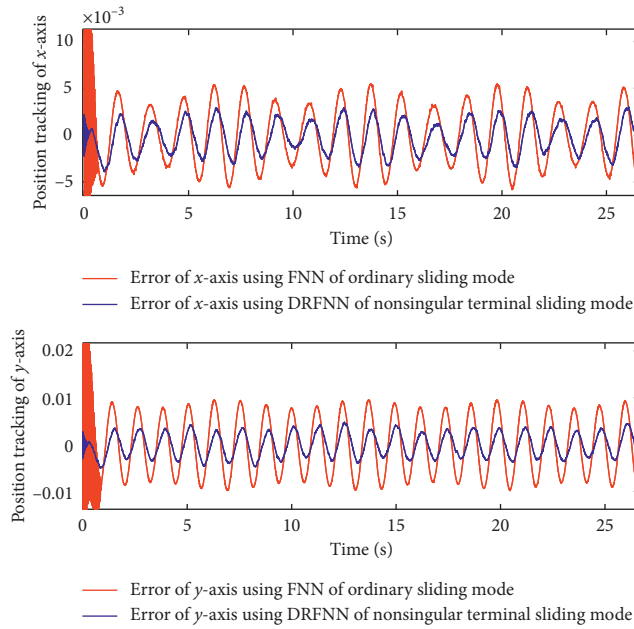
FIGURE 10: The comparison figure of the position tracking error.
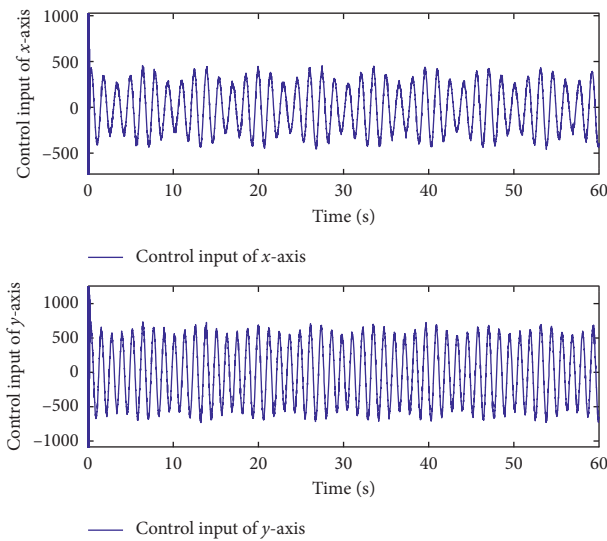
FIGURE 11: Output of the DRFNN on NTSMC.
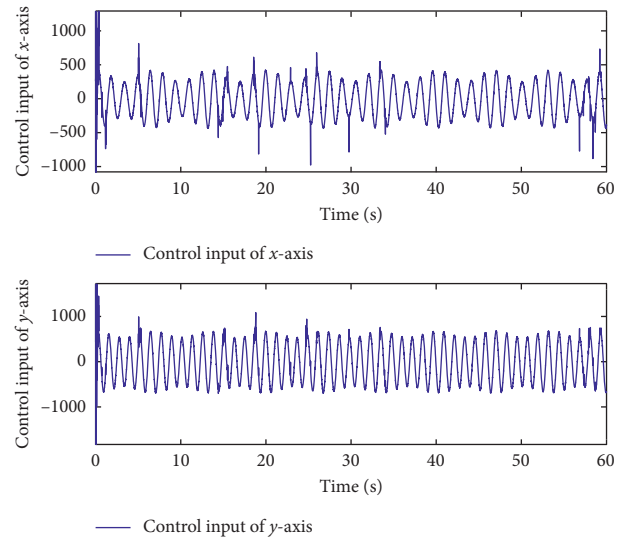
FIGURE 12: Output of the DRFNN on TSMC.

tracking error based on the DRFNN of NTSMC has faster convergence speed and smaller steady-state deviation, which shows the trajectories of the DRFNN of NTSMC are closer to the reference signal than those of the FNN of SMC.

Figure 11 is the performance curve of control force, which indicates that the input of the controller can be basically stable within a certain range. Figure 12 also adopts the DRFNN, but the sliding mode surface adopts the ordinary terminal sliding mode (TSMC). It can be seen that when the system state is in the subspace of a specific state space, the control signal of the TSMC may show undesired overshoots. By comparing Figures 11 and 12, it is shown that the NTSMC can effectively solve the above

singular problems, which coincides with the theoretical analysis.

Figure 13 is the dynamic figure of the sliding surface. It can be seen that the state trajectory of the sliding surface can rapidly converge to origin in a finite time, which indicates that the system can remain in a stable state even in the presence of model uncertainties and external disturbances. Figure 14 is the enlarged figure after the state trajectory of the DRFNN of NTSMC and the ordinary FNN of ordinary SMC are magnified in the same coordinate system. It can be seen from the comparison that the trajectory of the sliding surface of the NTSMC converges to the convergence region more rapidly; therefore, NTSMC can stabilize the system in a shorter time.
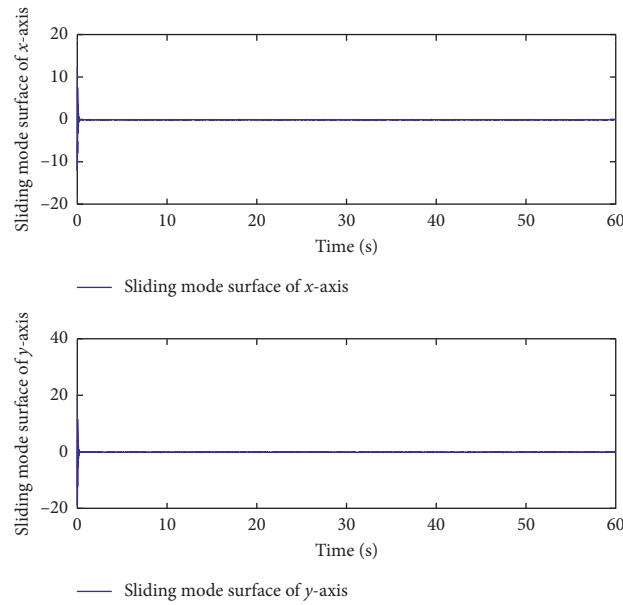
FIGURE 13: Sliding mode surface of the DRFNN on NTSMC.
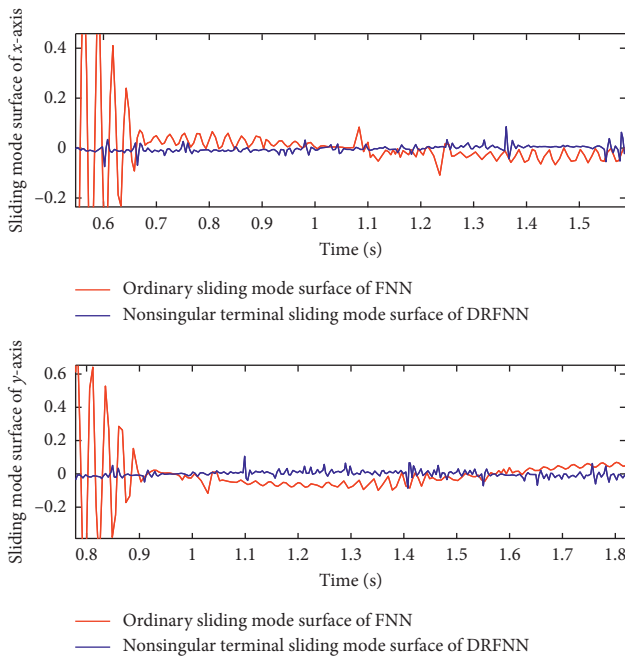
FIGURE 14: Comparison of the sliding surface.

FIGURE 15: The nonlinear term tracking.

Figure 15 is the output of the DRFNN for the estimation of the nonlinear term. It can be seen that the output of the DRFFN is consistent with the value of the nonlinear term. Figure 16 is the nonlinear term tracking error observed after amplification waveform in the same coordinate system based on the FNN of SMC and the DRFNN of NTSMC, respectively, showing that the output of the DRFNN can more quickly and accurately predict the actual value of the system uncertainties.

Figures 17–21 are the self-regulating waveforms of the five fully regulated parameters on the x-axis, respectively,

and Figures 22–26 are the self-regulating waveforms of the five fully regulated parameters on the y-axis, respectively. Both the x- and y-axis, the width vector, the center vector, the inner feedback gain, outer feedback gain, and the weight can quickly converge to a stable value, which suggests the joined internal and external layer of the feedback loop, and the proposed controller has outstanding adaptive ability.

The deviation degree of a group of measurement data from the real value can be reflected by the root mean square error (RMSE). The smaller the RMSE is, the higher the control precision is. The calculation formula of RMSE is
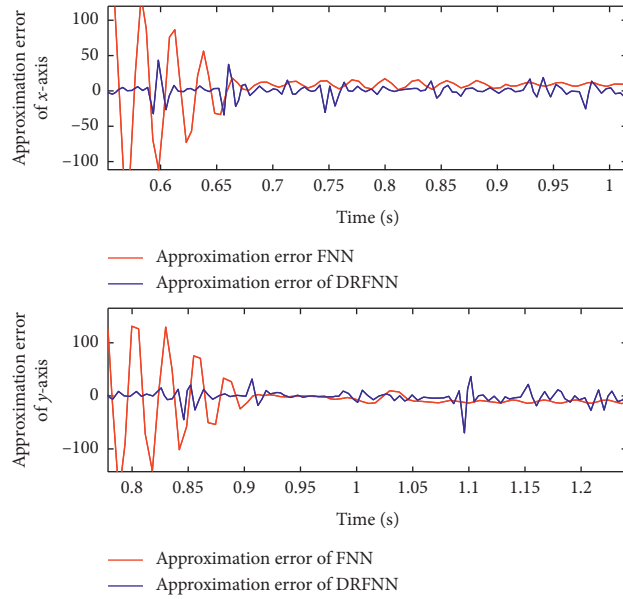
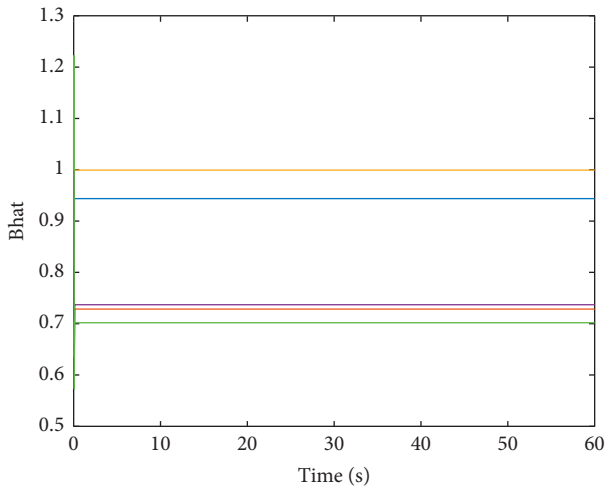Figure 16: Comparison diagram of the estimated errors.

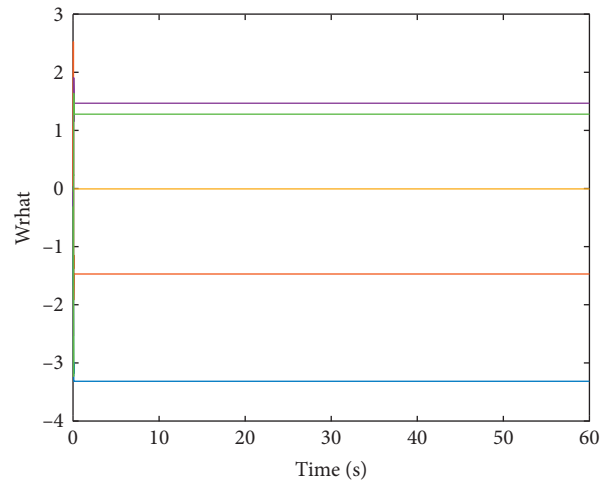Figure 17: The width vector self-adjusting figure of the x-axis.

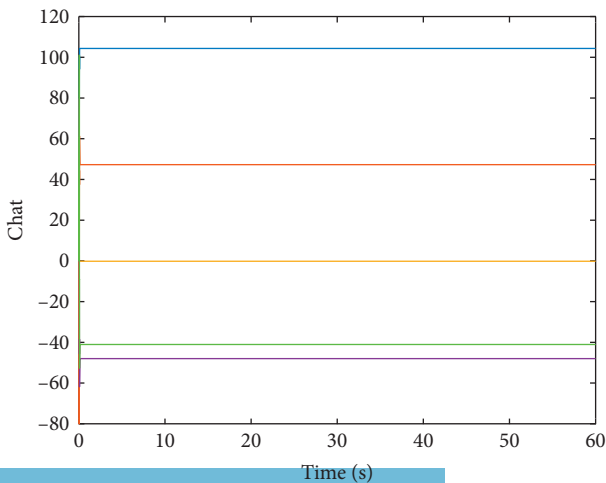Figure 19: The inner layer gain self-adjusting figure of the x-axis.

Figure 18: The center vector self-adjusting figure of the x-axis.
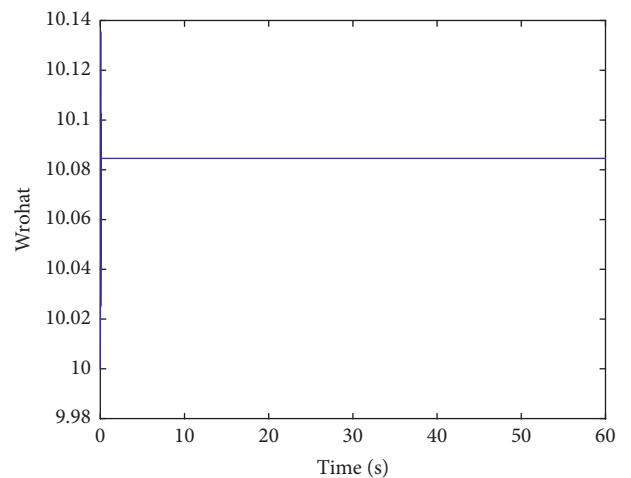

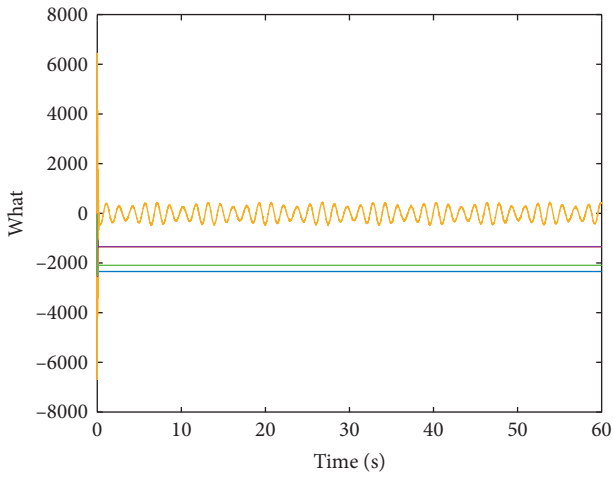Figure 20: The outer layer gain self-adjusting figure of the x-axis.

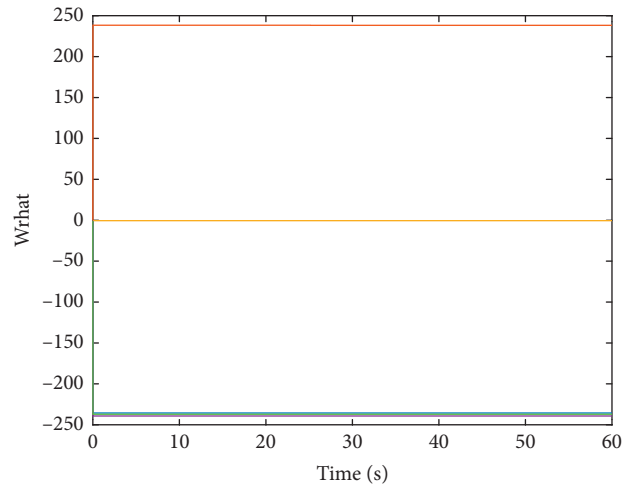Figure 21: The weight self-adjusting figure of the x-axis.

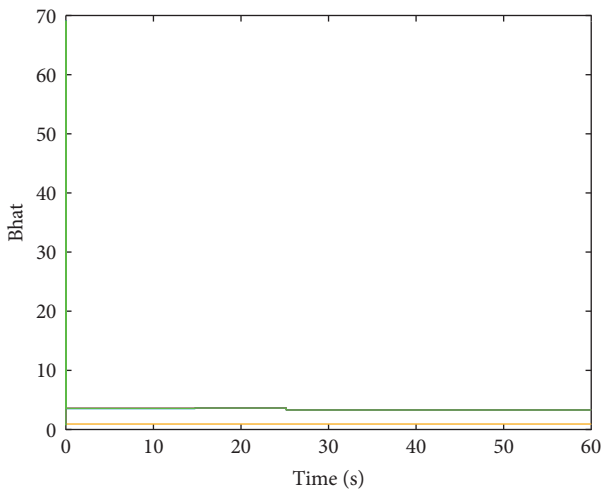Figure 24: The inner gain self-adjusting figure of the y-axis.

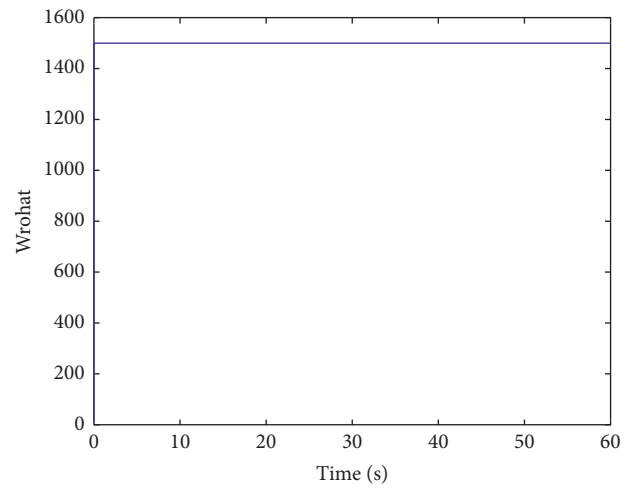Figure 22: The base width self-adjusting figure of the y-axis.

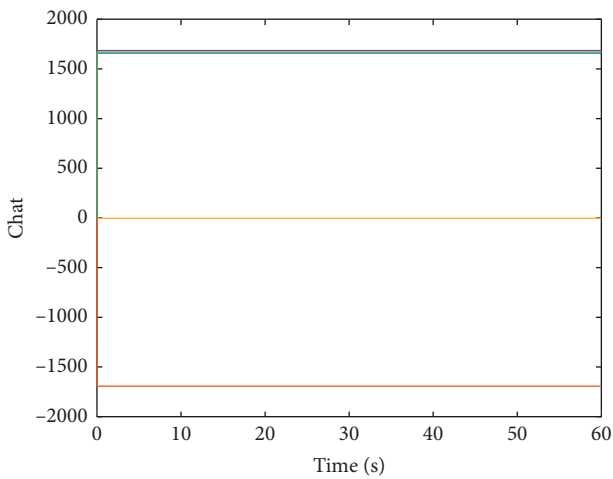Figure 25: The outer gain self-adjusting figure of the y-axis.

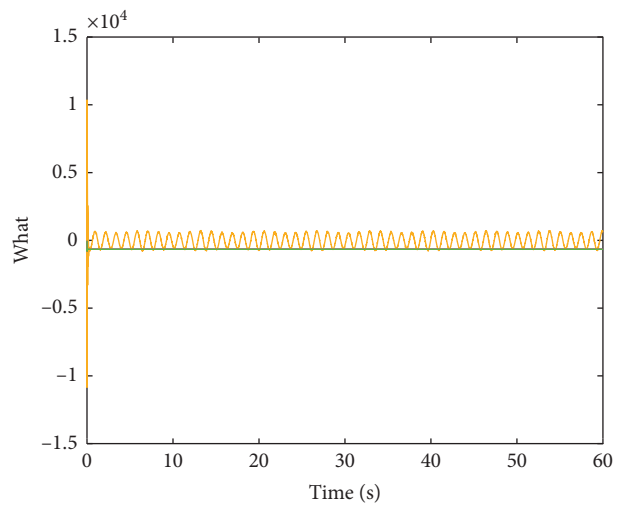Figure 23: The center vector self-adjusting figure of the y-axis.

Figure 26: The weight self-adjusting figure of the y-axis.

Table 1: Comparison of RMSE.

RMSE of two axes control method	X	Y
FNN of SMC	0.0032	0.0064
DRFNN of NTSMC	0.0011	0.0014

$$RMSE = sqrt\left(sum\left(\frac{(q_i - q_{ri})^2}{n} \right) \right), \tag{49}$$

where q_i is the calculated trace value, q_{ri} is the reference signal, and n is the sample number.

It can be intuitively seen from Table 1 that the RMSE obtained based on the DRFNN of NTSMC on the microgyroscope is smaller than that on the FNN of SMC. According to the above analysis and comparison results, the DRFNN of the NTSMC system has better desired control performance.

6. Conclusion

In this paper, we designed a double-loop recurrent fuzzy neural network of nonsingular terminal sliding mode control for the MEMS gyroscope system. First, we simplified the spatial structure model of the microgyroscope and derived the dynamic differential equation. Then, the nonsingular terminal sliding mode control scheme is employed to drive the state of the system to follow the desired trajectory in a finite period of time. Meanwhile, we eliminate the negative exponential term in the control rate, thus avoiding undesired singularities in terminal control law. Moreover, the DRFNN is introduced into the control strategy to compensate the nonlinear term, which adds two inner and outer feedback loops for guarantying the adaptability of the controller. According to the comparative results, the DRFNN of NTSMC has faster rate of reaction, higher tracking accuracy, and more accurate estimation of system uncertainties than the conventional control method. Therefore, the control strategy proposed in this paper can be effectively applied in the microgyroscope system.

Data Availability

The data used to support the findings of this study are included within the article.

Conflicts of Interest

The authors declare that there are no conflicts of interest regarding the publication of this paper.

Acknowledgments

References

[1] N. Yazdi, F. Ayazi, and K. Najafi, "Micromachined inertial sensors," *Proceedings of the IEEE*, vol. 86, no. 8, pp. 1640–1659, 1998.

[2] H. Liu, L. Feng, Z. Jiao, and R. Li, "Polarization noise and reduction technology in micro optical gyroscope," in *Proceedings of the 6th IEEE International Conference on Nano/Micro Engineered and Molecular Systems*, pp. 956–959, Kaohsiung, Taiwan, February 2011.

[3] J. Raman, E. Cretu, P. Rombouts, and L. Weyten, "A closed-loop digitally controlled MEMS gyroscope with unconstrained sigma-delta force-feedback," *IEEE Sensors Journal*, vol. 9, no. 3, pp. 297–305, 2009.

[4] M. Rahmani, H. Komijani, A. Ghanbari, and M. M. Ettefagh, "Optimal novel super-twisting PID sliding mode control of a MEMS gyroscope based on multi-objective bat algorithm," *Microsystem Technologies*, vol. 24, no. 6, pp. 2835–2846, 2018.

[5] M. Fazlyab, M. Z. Pedram, H. Salarieh, and A. Alasty, "Parameter estimation and interval type-2 fuzzy sliding mode control of a z-axis MEMS gyroscope," *ISA Transactions*, vol. 52, no. 6, pp. 900–911, 2013.

[6] J. Y. Hung, W. Gao, and J. C. Hung, "Variable structure control: a survey," *IEEE Transactions on Industrial Electronics*, vol. 40, no. 1, pp. 2–22, 1993.

[7] V. I. Utkin, "Sliding mode control design principles and applications to electric drives," *IEEE Transactions on Industrial Electronics*, vol. 40, no. 1, pp. 23–36, 1993.

[8] L. Wang, T. Chai, and L. Zhai, "Neural-network-based terminal sliding-mode control of robotic manipulators including actuator dynamics," *IEEE Transactions on Industrial Electronics*, vol. 56, no. 9, pp. 3296–3304, 2009.

[9] C.-C. Wang and H.-T. Yau, "Nonlinear dynamic analysis and sliding mode control for a gyroscope system," *Nonlinear Dynamics*, vol. 66, no. 1-2, pp. 53–65, 2011.

[10] L. Qiao and W. Zhang, "Adaptive second-order fast nonsingular terminal sliding mode tracking control for fully actuated autonomous underwater vehicles," *IEEE Journal of Oceanic Engineering*, vol. 44, no. 2, pp. 363–385, 2019.

[11] D. H. Shah and D. M. Patel, "Design of sliding mode control for quadruple-tank MIMO process with time delay compensation," *Journal of Process Control*, vol. 76, pp. 46–61, 2019.

[12] J. Fei and Z. Feng, "Adaptive fuzzy super-twisting sliding mode control for microgyroscope," *Complexity*, vol. 2019, Article ID 6942642, 13 pages, 2019.

[13] S. T. Venkataraman and S. Gulati, "Control of nonlinear systems using terminal sliding modes," in *Proceedings of the 1992 American Control Conference*, pp. 891–893, Chicago, IL, USA, June 1992.

[14] Z. Man, A. Paplinski, and H. R. Wu, "A robust MIMO terminal sliding mode control scheme for rigid robotic manipulators," *IEEE Transactions on Automatic Control*, vol. 39, no. 12, pp. 2464–2469, 1995.

[15] C.-K. Lin, "Nonsingular terminal sliding mode control of robot manipulators using fuzzy wavelet networks," *IEEE Transactions on Fuzzy Systems*, vol. 14, no. 6, pp. 849–859, 2006.

[16] A. Ghanbari and M. R. Moghanni-Bavil-Olyaei, "Adaptive fuzzy terminal sliding-mode control of MEMS z-axis gyroscope with extended Kalman filter observer," *Systems Science & Control Engineering*, vol. 2, no. 1, pp. 183–191, 2014.

[17] L. Qiao and W. Zhang, "Double-loop integral terminal sliding mode tracking control for UUVs with adaptive dynamic

compensation of uncertainties and disturbances," *IEEE Journal of Oceanic Engineering*, vol. 44, no. 1, pp. 29–53, 2019.

[18] Y. Fang, J. Fei, and D. Cao, "Adaptive fuzzy-neural fractional-order current control of active power filter with finite-time sliding controller," *International Journal of Fuzzy Systems*, vol. 21, no. 5, pp. 1533–1543, 2019.

[19] D. Ma and H. Lin, "Chattering-free nonsingular fast terminal sliding-mode control for permanent magnet synchronous motor servo system," in *Proceedings of the 2016 35th Chinese Control Conference*, pp. 3463–3467, Chengdu, China, July 2016.

[20] S. Hou, J. Fei, and C. Chen, "Finite-time adaptive fuzzy-neural-network control of active power filter," *IEEE Transactions on Power Electronics*, vol. 34, no. 10, pp. 1941–0107, 2019.

[21] J. Fei and H. Ding, "Adaptive sliding mode control of dynamic system using RBF neural network," *Nonlinear Dynamics*, vol. 70, no. 2, pp. 1563–1573, 2012.

[22] C.-T. Lin and C. S. G. Lee, "Neural-network-based fuzzy logic control and decision system," *IEEE Transactions on Computers*, vol. 40, no. 12, pp. 1320–1336, 1991.

[23] Y. Zhu and J. Fei, "Disturbance observer based fuzzy sliding mode control of PV grid connected inverter," *IEEE Access*, vol. 6, pp. 21202–21211, 2018.

[24] J. Fei and J. Zhou, "Robust adaptive control of MEMS triaxial gyroscope using fuzzy compensator," *IEEE Transactions on Systems, Man, and Cybernetics, Part B (Cybernetics)*, vol. 42, no. 6, pp. 1599–1607, 2012.

[25] J. Fei and H. Wang, "Experimental investigation of recurrent neural network fractional-order sliding mode control for active power filter," *IEEE Transactions on Circuits and Systems II-Express Briefs*, 2019.

[26] J. Fei and X. Liang, "Adaptive backstepping fuzzy neural network fractional-order control of microgyroscope using a nonsingular terminal sliding mode controller," *Complexity*, vol. 2018, Article ID 5246074, 12 pages, 2018.

[27] C.-H. Lee and C.-C. Teng, "Identification and control of dynamic systems using recurrent fuzzy neural networks," *IEEE Transactions on Fuzzy Systems*, vol. 8, no. 4, pp. 349–366, 2000.

[28] J. Fei and Y. Chu, "Double hidden layer recurrent neural adaptive global sliding mode control of active power filter," *IEEE Transactions on Power Electronics*, 2019.

[29] Y. Chu, J. Fei, and S. Hou, "Adaptive global sliding mode control for dynamic systems using double hidden layer recurrent neural network structure," *IEEE Transactions on Neural Network and Learning System*, 2019.

[30] J. Fei and C. Lu, "Adaptive sliding mode control of dynamic systems using double loop recurrent neural network structure," *IEEE Transactions on Neural Networks and Learning Systems*, vol. 29, no. 4, pp. 1275–1286, 2018.

[31] X. Huikai and G. K. Fedder, "Fabrication, characterization, and analysis of a DRIE CMOS-MEMS gyroscope," *IEEE Sensors Journal*, vol. 3, no. 5, pp. 622–631, 2003.

[32] P. Sungsu and R. Horowitz, "Adaptive control for z-axis MEMS gyroscopes," in *Proceedings of the 2001 American Control Conference*, pp. 1223–1228, Arlington, VA, USA, June 2001.

[33] Y. Fang, J. Fei, and Y. Yang, "Adaptive backstepping design of a microgyroscope," *Micromachines*, vol. 9, no. 7, p. 338, 2018.